Analytic evaluation of hydrogen neutron elastic scattering moments with free-gas thermal treatment compared to NJOY

Yunhuang Zhang [*], Marvin L. Adams [**]

Department of Nuclear Engineering, Texas A&M University College Station, TX, 77843, USA

A B S T R A C T

In this paper, we present an analytic approach to evaluate Legendre moments of hydrogen neutron elastic scattering differential cross section, with and without free-gas thermal treatment. The results for the zero-th (P_0) and first (P_1) moments are given and compared against a 138-group cross sections produced by NJOY. An MCNP thin-wire test was employed as an independent verification for our analytic model for the free-gas zero-th moment. Excellent agreement was observed between the analytic result and MCNP prediction. They both suggest that an increased thermal cut-off in NJOY THERMR module is advisable for higher accuracy. Discrepancy was also found between the analytic model and NJOY multi-group cross section for the first order Legendre moments of the differential cross section, which might indicate a numerical anomaly in NJOY.

1. Introduction

Accurate neutron cross sections are fundamental to accurate neutron transport calculation. Raw cross section data from the Evaluated Nuclear Data Files (ENDF) has to be processed in one way or another before it can be used in specific transport codes. For instance, MCNP in continuous energy mode requires continuous-energy cross sections in ACE format, while deterministic transport codes, in general, call for multi-group cross sections. NJOY (MacFarlane, 2013) is comprehensive computer code package for producing point-wise and multi-group nuclear cross sections and related quantities from the ENDF files. During the process, the cross section data flows through a sequence of NJOY modules dedicated to different physics phenomenon, such as Doppler broadening, thermal scattering, and shelf-shielding, just to name a few. NJOY is well respected and used throughout particle transport community, and was regarded as the 'gold standard' for generating multi-group cross sections (Conlin et al., 2017). However, since the original NJOY was written in 1970s (Conlin et al., 2017) with very limited computing power accessible, many of its algorithms were optimized for efficiency rather than accuracy. Nowadays, with vastly improved computers the community is pushing for higher simulation fidelity. It perfectly logical to re-evaluate NJOY's accuracy and its implication for simulation results. In this paper, we limit our investigation to NJOY2012, whose kernel is shared by the more recent releases,

NJOY2016 and NJOY21. We focuses on hydrogen elastic scattering cross sections for two reasons. First, neutron-hydrogen scattering is the most important thermal scattering in modern thermal reactors moderated by either light water or heavy water. Secondly, neutron-hydrogen scattering is amenable to the classic two-body kinematics and is known to be isotropic in the center-of-mass (CoM) frame. The two-body kinematics model allows us to obtain analytic expressions for the scattering Legendre moments as a function of incident and emerging neutron energies, with or without free-gas treatment. Those analytic expressions serve as solid benchmarks for verifying NJOY's multi-group scattering transfer matrices. Besides the analytic model, we also employed MCNP as an independent verification for the free-gas treatment for the P_0 moment. MCNP is a transport code based on monte-carlo method, in which each particle's random walk is simulated and tracked. For that reason, MCNP uses its own physics model for free-gas treatment rather than relying on thermal cross sections given by the cross section libraries (Zhang et al., 2017) and therefore serves as an excellent independent reference. For this research, we used the latest version of MCNP6. In the remainder of this paper, we will drop the code version number and refer to NJOY2012 and MCNP6 as NJOY and MCNP, respectively.

1.1. Analytic model: two-body kinematics

The analytic model we use in this paper is based on the classic two-

body kinematics. Two-body kinematics has been used to model neutron energy transfer in an elastic scattering event when the target nuclei are at rest (static) (Lamarsh and Baratta, 2001) or subject to free-gas thermal motion (Bell and Glasstone, 1985). However, to the authors' knowledge there was no systematic derivation for secondary energy distribution associated with arbitrary order of Legendre moments base on this model. In this paper we show it is possible to obtain analytic expressions for those secondary energy distributions, with and without free-gas thermal treatment. In the two-body kinematics model, two particles carry certain initial velocities before collision (scattering) and their kinetic energies and momenta get redistributed afterwards. In this process, the system's total kinetic energy and momentum are conserved. In the rest of this paper, we will refer to kinetic energy by simply 'energy'. First, let's introduce some nomenclatures that will be used throughout the discussion:

$\vec{v}_l$	incident neutron velocity in lab frame,
$\vec{V}_l$	initial target nucleus velocity in lab frame,
Φ	approaching angle in lab frame (between $\vec{v}_l$ and $\vec{V}_l$),
M	neutron mass,
M	target nucleus mass,
A	target-to-neutron mass ratio ($A = M/m$),
$\vec{v}_o$	center-of-mass velocity in lab frame,
$\vec{v}_c$	incident neutron velocity in CoM frame,
$\vec{V}_c$	initial target nucleus velocity in CoM frame,
$\vec{v}'_c$	emerging neutron velocity in CoM frame,
$\vec{V}'_c$	emerging target nucleus velocity in CoM frame,
$\vec{v}'_l$	emerging neutron velocity in lab frame,
$\vec{V}'_l$	emerging target nucleus velocity in lab frame,
θ	neutron emerging angle in lab frame (between $\vec{v}_l$ and $\vec{v}'_l$),
μ	$= \cos(\theta)$,
ϑ	neutron emerying angle in CoM frame (between $\vec{v}_o$ and $\vec{v}'_c$),
ζ	CoM flight angle observed in lab frame (between $\vec{v}_l$ and $\vec{v}_o$),
E'	emerging neutron energy ($=\frac{1}{2}mv'^2_l$)

An illustration of the two-body kinematics model as observed in the lab frame is given in Fig. 1.

With the aforementioned nomenclature, the speed of center-of-mass can be computed as (for derivation we refer readers to (Bell and Glasstone, 1985)):

$$v_o = \frac{\sqrt{v_l^2 + A^2 V_l^2 + 2A v_l V_l \cos\phi}}{1 + A} \ . \tag{1}$$

With "s-wave" isotropic scattering in the CoM frame, ϑ is uniformly distributed from 0 to π. For a given ϑ, the speed of the emerging neutron can be computed using conservation of energy and conservation of momentum (Bell and Glasstone, 1985):

$$v'^2_l = \frac{A^2\left(v_l^2 + V_l^2 - 2v_l V_l \cos\phi\right)}{(1+A)^2} + \frac{v_l^2 + A^2 V_l^2 + 2A v_l V_l \cos\phi}{(1+A)^2}$$
$$+ \frac{2A\sqrt{v_l^2 + V_l^2 - 2v_l V_l \cos\phi}\sqrt{v_l^2 + A^2 V_l^2 + 2A v_l V_l \cos\phi}}{(1+A)^2} \cos(\vartheta) \ . \tag{2}$$
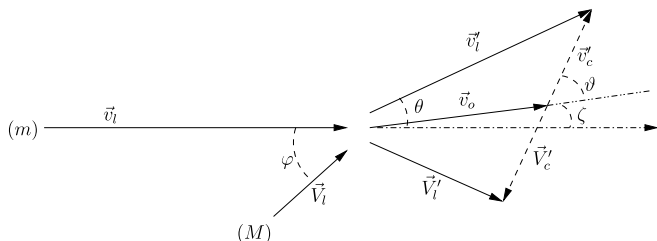

Fig. 1. Elastic scattering of neutron by nucleus, as observed in lab frame.

According to Eq. (2), the maximum v'_l is attained when $\vartheta = 0$. For given A, v_l, V_l, the maximum v'_l as a function of ϕ can be obtained as:

$$\max_{[A,v_l,V_l,\phi]}(v'_l) = \sqrt{v'^2_c + v_o^2 + 2v'_c v_o} = v'_c + v_o \tag{3}$$

$$= \frac{A\sqrt{v_l^2 + V_l^2 - 2v_l V_l \cos\phi} + \sqrt{v_l^2 + A^2 V_l^2 + 2A v_l V_l \cos\phi}}{1 + A} \ . \tag{4}$$

In the special case of neutron-hydrogen scattering, if we neglect the excess masses of neutron and hydrogen, then $A = 1$, and the maximum of v'_l of $\sqrt{v_l^2 + V_l^2}$ is obtained when $\phi = \pi/2$, which means the two initial particles were traveling perpendicular to each other before collision.

Similarly, the minimum v'_l is attained when $\vartheta = 2\pi$. For given A, v_l, V_l, the minimum v'_l as a function of ϕ can be obtained as:

$$\min_{[A,v_l,V_l,\phi]}(v'_l) = \sqrt{v'^2_c + v_o^2 - 2v'_c v_o} = |v'_c - v_o| \tag{5}$$

$$= \frac{\left|A\sqrt{v_l^2 + V_l^2 - 2v_l V_l \cos\phi} - \sqrt{v_l^2 + A^2 V_l^2 + 2A v_l V_l \cos\phi}\right|}{1 + A} \ . \tag{6}$$

In the special case of neutron-hydrogen scattering, $A = 1$, and the minimum of v'_l of zero can obtained when $\phi = \pi/2$, which is exactly the same case as for the maximum v'_l.

Let $p_{[A,v_l,V_l,\phi]}(E')$ denote the probability distribution function for emerging neutron energy E', which is parameterized by A, v_l, V_l, and ϕ. It is non-zero only between $\max_{[A,v_l,V_l,\phi]}(E')$ and $\min_{[A,v_l,V_l,\phi]}(E')$. According to Eq. (2), E' and scattering angle ϑ are directly associated. Therefore, the probability that a neutron emerges with energy E' is the same probability that a neutron emerges with a scattering angle of ϑ. That is:

$$p_{[A,v_l,V_l,\phi]}(E')dE' = -\frac{\sigma_s(\vartheta)}{\sigma_s}2\pi\sin\vartheta d\vartheta \ . \tag{7}$$

From Eq. (2), we have:

$$\frac{dE'}{d\vartheta} = \frac{1}{2}m\frac{2A\sqrt{v_l^2 + V_l^2 - 2v_l V_l \cos\phi}\sqrt{v_l^2 + A^2 V_l^2 + 2A v_l V_l \cos\phi}}{(1+A)^2}\sin\vartheta \ . \tag{8}$$

Because scattering is isotropic in CoM:

$$\sigma_s(\vartheta) = \frac{\sigma_s}{4\pi} \ , \tag{9}$$

Substituting Eq. (8) and Eq. (9) into Eq. (7), we obtain the expression for $p_{[A,v_l,V_l,\phi]}(E')$:

$$p_{[A,v_l,V_l,\phi]}(E') = \frac{(1+A)^2}{2mA\sqrt{v_l^2 + V_l^2 - 2v_l V_l \cos\phi}\sqrt{v_l^2 + A^2 V_l^2 + 2A v_l V_l \cos\phi}}\frac{4\pi\sigma_s(\vartheta)}{\sigma_s} \ . \tag{10}$$

To facilitate the energy transfer analyses, let's re-express v_l and V_l parameterization in terms of E and E_p:

$$p_{[A,E,E_p,\phi]}(E') = \frac{(1+A)^2}{4\sqrt{A^2 E + AE_p - 2\sqrt{A^3 E \cdot E_p}\cos\phi}\sqrt{E + AE_p + 2\sqrt{AE \cdot E_p}\cos\phi}} \ , \tag{11}$$

for $\max_{[A,E,E_p,\phi]}(E') \leq E' \leq \min_{[A,E,E_p,\phi]}(E')$, where:

$$\max_{[A,E,E_p,\phi]}(E') = \frac{A^2 E + AE_p - 2\sqrt{A^3 E \cdot E_p}\cos\phi}{(1+A)^2} + \frac{E + AE_p + 2\sqrt{AE \cdot E_p}\cos\phi}{(1+A)^2}$$
$$+ 2\frac{\sqrt{A^2 E + AE_p - 2\sqrt{A^3 E \cdot E_p}\cos\phi}\sqrt{E + AE_p + 2\sqrt{AE \cdot E_p}\cos\phi}}{(1+A)^2} \ , \tag{12}$$

$$\min_{[A,E,E_p,\phi]}(E') = \frac{A^2E + AE_p - 2\sqrt{A^3E \cdot E_p}\cos\phi}{(1+A)^2} + \frac{E + AE_p + 2\sqrt{AE \cdot E_p}\cos\phi}{(1+A)^2}$$

$$-2\frac{\sqrt{A^2E + AE_p - 2\sqrt{A^3E \cdot E_p}\cos\phi}\sqrt{E + AE_p + 2\sqrt{AE \cdot E_p}\cos\phi}}{(1+A)^2} . \quad (13)$$

1.2. Secondary energy distribution for P_0 moment with free-gas treatment

Free-gas model entails that E_p is subject to the Maxwellian distribution $f_{T_p}(E_p)$ and ϕ is subject to an isotropic distribution $g(\phi)$:

$$f_{T_p}(E_p) = 2\sqrt{\frac{E_p}{\pi}}\left(\frac{1}{kT_p}\right)^{3/2}\exp\left(\frac{-E_p}{kT_p}\right) , \quad (14)$$

$$g(\phi) = 1/4\pi , \quad (15)$$

where k is the Boltzmann constant ($k = 8.6173324 \times 10^{-5}eV\cdot K^{-1}$) and T_p is the target material temperature. To compute the secondary (emerging) energy distribution for P_0 moment with free-gas treatment, we need to take the thermal motion of target nuclei into account by integrating Eq. (11) over all possible E_p and ϕ, weighted by their probability distribution functions respectively:

$$P_0(E \rightarrow E') = \int_0^\infty f_{T_p}(E_p)\int_0^\pi g(\phi)2\pi\sin\phi\, p_{[A,E,E_p,\phi]}(E')d\phi dE_p . \quad (16)$$

1.3. Secondary energy distribution for P_1 moment with & without free-gas treatment

The model for P_1 moment secondary energy distribution entails one more complication as compared to the P_0 case, that is the neutron emerging angle in lab frame. First, it can be shown that there is a one-to-one correspondence between θ_o and E', where θ_o is the angle between $\vec{v}'_l$ and $\vec{v}_o$, as illustrated in Fig. 2.

Given a set of parameters A, E, E_p, and ϕ, the relationship between $\cos(\theta_o)$ and E' can be expressed as:

$$\cos(\theta_o) = \frac{(1+A)^2E' + (1-A^2)E + 2\left(\sqrt{A} + \sqrt{A^3}\right)\sqrt{E \cdot E_p}\cos\phi}{2\sqrt{E + AE_p + 2\sqrt{AE \cdot E_p}\cos\phi}\cdot\sqrt{(1+A)^2E'}} . \quad (17)$$

Also, $\cos(\zeta)$ can be computed as:

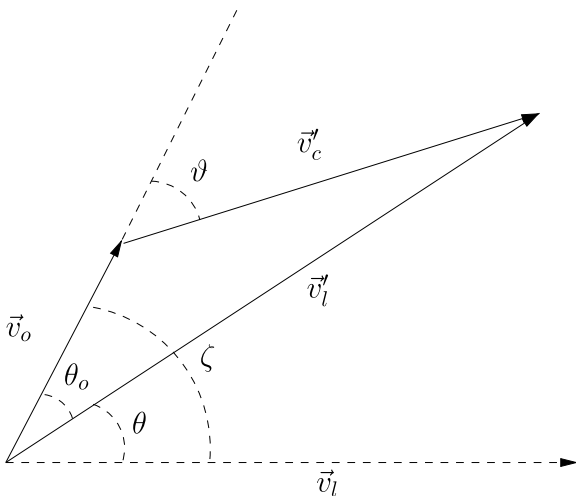$$\cos(\zeta) = \frac{v_l + AV_l\cos(\phi)}{\sqrt{v_l^2 + A^2V_l^2 + 2Av_lV_l\cos(\phi)}} . \quad (18)$$

It appears in Fig. 2 that $\vec{v}_l$, $\vec{v}_o$, and $\vec{v}'_l$ are all in the same plane. However, this is not true in general. In CoM frame, the scattered neutron flight direction is prescribed not only by the polar angle (ϑ) with respect to $\vec{v}_o$, but also by an azimuthal angle ω, which is the angle between the plane defined by $\vec{v}_l$ and $\vec{v}_o$ and the plane defined by $\vec{v}_o$ and $\vec{v}'_l$. An illustration of the relationship between angles θ, θ_o, ζ, and ω is shown in Fig. 3. Eq. (19) gives an expression for μ in terms of the other three angles.

$$\mu \equiv \cos\theta = \left(1 + \sqrt{1/\cos^2(\theta_o) - 1}\sqrt{1/\cos^2(\zeta) - 1}\cos\omega\right)\cos\theta_o\cos\zeta . \quad (19)$$

Combining Eq. (17), Eq. (18), and Eq. (19), we can see that for a given set of parameters (A, E, E_p, E', ϕ), μ is dependent on ω. It is reasonable to assume ω is uniformly distributed between 0 and 2π as the scattering is isotropic in CoM frame. Therefore ω is subject to the following distribution:

$$h(\omega) = \frac{1}{2\pi} . \quad (20)$$

To compute secondary energy distribution for P_1 moment with free-gas treatment, we need to perform the similar integration as shown in Eq. (16), except that we also need to integrate over μ with the weighting being μ itself times its probability distribution:

$$P_1(E \rightarrow E') = \int_0^\infty f_{T_p}(E_p)\int_0^\pi g(\phi)2\pi\sin\phi\, p_{[A,E,E_p,\phi]}(E')$$
$$\int_{-1}^1 \mu q_{[A,E,E_p,E',\phi]}(\mu)d\mu d\phi dE_p , \quad (21)$$

where $q_{[A,E,E_p,E',\phi]}(\mu)$ is the μ distribution parameterized by A, E, E_p, E', and ϕ. Unfortunately, it is not easy to establish $q(\mu)$. An alternative approach is to substitute μ with ω, which is uniformly distributed. With this substitution, Eq. (21) can be rewritten as:

$$P_1(E \rightarrow E') = \int_0^\infty f_{T_p}(E_p)\int_0^\pi g(\phi)2\pi\sin\phi\, p_{[A,E,E_p,\phi]}(E')$$
$$\int_0^{2\pi} \mu_{[A,E,E_p,E',\phi]}(\omega)h(\omega)d\omega d\phi dE_p , \quad (22)$$

where $\mu(\omega)$ is obtained by substituting Eq. (17) and Eq. (18) into Eq. (19).

Computing secondary energy distribution for P_1 moment without thermal treatment (static) is much less complicated. First of all, integration over E_p and ϕ is dropped, and we only need to evaluate distributions at $E_p = 0$. Furthermore, since target nucleus is at rest ($V_l = 0$),
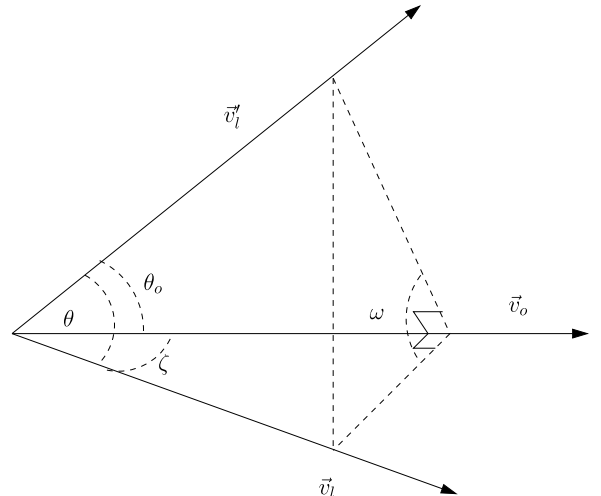

Fig. 2. Emerging neutron angles as observed in different coordinates.

Fig. 3. Relationship between θ, θ_o, ζ, and ω

$\overrightarrow{v}_o$ is parallel to $\overrightarrow{v}_l$, which means θ_o becomes θ. It greatly simplifies the expression for μ:

$$\mu \equiv \cos\theta = \cos\theta_o = \frac{(1+A)^2 E' + (1-A^2)E + 2\left(\sqrt{A} + \sqrt{A^3}\right)\sqrt{E \cdot E_p}\cos\phi}{2\sqrt{E + AE_p + 2\sqrt{AE \cdot E_p}\cos\phi} \cdot \sqrt{(1+A)^2 E'}} .$$

(23)

In this case μ no longer depends on ω and there is only one possible μ value for each energy pair $(E \to E')$. That is, $q(\mu)$ is a Dirac delta function:

$$q_{[A,E,E_p=0,E']}(\mu) = \delta\left(\mu - \mu_{[A,E_p=0]}(E \to E')\right) .$$

(24)

Therefore, the secondary energy distribution can be computed as:

$$P_1(E \to E') = p_{[A,E,E_p=0]}(E') \int_{-1}^{1} \mu \, q_{[A,E,E_p=0,E']}(\mu) d\mu$$

(25)

$$= p_{[A,E,E_p=0]}(E') \mu_{[A,E_p=0]}(E \to E') .$$

(26)

1.4. Secondary energy distribution for higher order moments

The discussion presented in Section 2.2 can be generalized to higher order moments. To compute secondary energy distributions for higher moments, one only needs to replace μ with $P_\ell(\mu)$ in Eq. (22) for free-gas case and Eq. (26) for static case, where ℓ is the Legendre order desired.

2. P_0 Secondary energy distribution for hydrogen scattering

We tested our analytic model for P_0 secondary distribution in the case of hydrogen scattering, and compared the results with both continuous energy and multi-group cross sections produced by NJOY. The material temperature (T_p) was set to be room temperature of 296 K.

2.1. Analytic model vs continuous energy cross section

The first comparison we performed was analytic model vs. continuous energy cross section generated by NJOY. The continuous energy cross section was generated in the ACE format that can be used by monte-carlo codes such as MCNP and SERPENT, using raw data from ENDF/B-VII.1 library with *emax* = 10eV. *emax* is a parameter in NJOY's THERMR module that specifies the maximum incident neutron energy up to which thermal treatment will be applied. It is a common practice to set *emax* to anywhere from 0.1 to 10.0 eV. The common wisdom is that thermal effect will be most prominent when neutron energy is comparable to the kinetic energy (0.025 eV at room temperature) of the target nuclei or/and below molecules binding energy in the target materials, both of which are usually below 10.0eV. One immediate difficulty associated with continuous energy cross section is that the secondary energy distribution is not directly available from the cross section itself due to its continuous energy nature. As a walk-around we built a thin-wire test problem in MCNP to infer the secondary energy distribution from the cross section for a series of discrete incident neutron energies. The thin-wire is made of target material, hydrogen in this case. Normally incident mono-energetic neutrons come in from the left end and propagate through the wire. The wire has a very large aspect ratio. It measures 10^{-12} mean-free-paths (mfp) in cross sectional diameter and 10^6 mfp's in total length. The large aspect ratio ensures that whenever a neutron has its first collision (scattering) with the material, it changes direction and will fly across the wire surface. We then tally the neutron current passing through the surface by energy bins, which will give us an estimate of the first-collided neutron energy spectrum. The spectrum, as shown in Eq. (27), is proportional to the secondary neutron energy distribution:

$$P_0(E \to E') \propto \sigma_s(E \to E')\varphi(E) = \lim_{\substack{R \to 0 \\ L \to \infty}} \oiint J(E') dA$$

(27)

An illustration of the thin-wire test set-up is given in Fig. 4.

The results are shown in Fig. 5, where comparison are made for incident energy of 0.1eV, 0.95eV, 9.5eV, and 78eV, respectively.

It can be seen from Fig. 5 that continuous energy results are highly consistent with our analytic model's prediction, which gives us confidence in both methods. Besides that, two more observations need to be pointed out:

- There is consistent curve-down towards the low energy end for each incident energy plotted. The curve-down shows the thermal treatment effect and it is observed to be on similar relative scale across the entire incident energy range. This observation contradicts the intuition that thermal treatment is only applicable to incident neutrons with energy lower than 10eV.
- Although NJOY *emax* was set to be 10eV, thermal treatment was observed from continuous energy results higher than 10eV. It means MCNP uses on its own free-gas model for thermal treatment, rather than relying on the thermal scattering data in the cross section data.

2.2. Continuous energy cross section vs multi-group cross section

With the success of verifying continuous energy cross section against our analytic model, we move on to the next test: continuous energy cross section vs multi-group cross section. The secondary energy distributions can be directly extracted from the multi-group cross section data as they are simply the columns of the scattering transfer matrix. The multi-group cross sections we used here were also generated by NJOY using the same ENDF/B-VII.1 library. Prompted by the finding in the previous test, we raised *emax* to 100eV. The results are shown in Fig. 6.

It can be seen from Fig. 6 that multi-group cross section agree with continuous energy cross section very well up to incident energy of 9.5eV. Interestingly, for incident energies above 9.5eV, the multi-group cross section reverts back to its static form, that is, the secondary energy is uniformly distributed from 0 to incident energy (Lamarsh and Baratta, 2001). It shows that NJOY has its hard-coded limit on the thermal cut-off, which was later verified to be 10eV through our communication with Los Alamos National Laboratory (LANL). Above this limit, NJOY does not apply any form of thermal treatment even if the user-specified *emax* value is higher than that. Another observation is that for very high incident energies (around MeV range), there appears to be some oscillations near the low energy end. This could be attributed to numerical artifacts associated with NJOY's angular integration scheme (Zheng and McClarren, 2015).

We further extended our discussion to include a test on $S(\alpha, \beta)$ treatment for hydrogen. In addition to thermal motion, $S(\alpha, \beta)$ treatment accounts for molecule binding effect and lattice effect caused by target material's crystalline structure. In this particular case, we looked at the $S(\alpha, \beta)$ effect for hydrogen bonded in high density polyethylene (HDPE). The results are shown in Fig. 7.

Similar to the case of free-gas hydrogen, multi-group cross section only receives thermal treatment for incident energies up to 10eV, albeit *emax* was set to be 100eV. Continuous energy cross section still receives thermal treatment across the entire energy range. Unlike in the case of
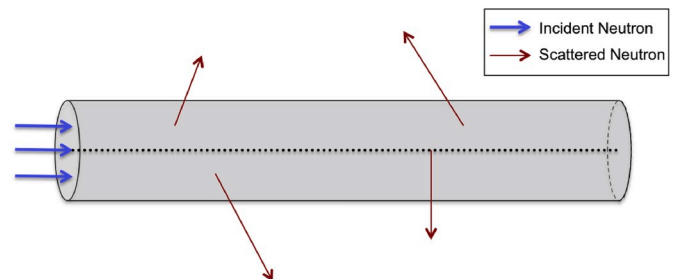

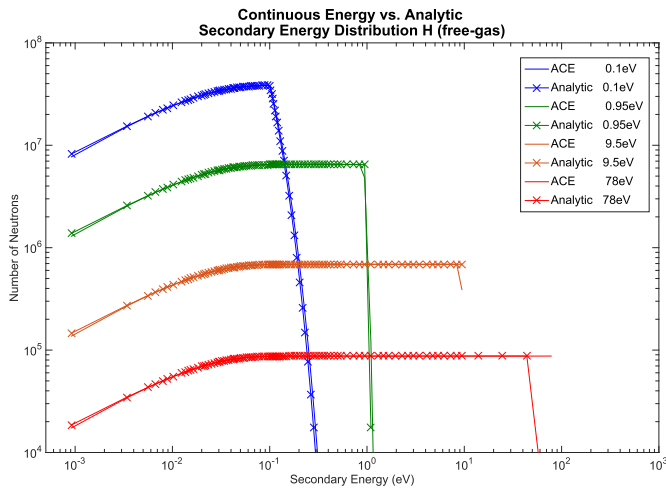**Fig. 4.** Thin-wire simulation illustration (not drawn to scale).

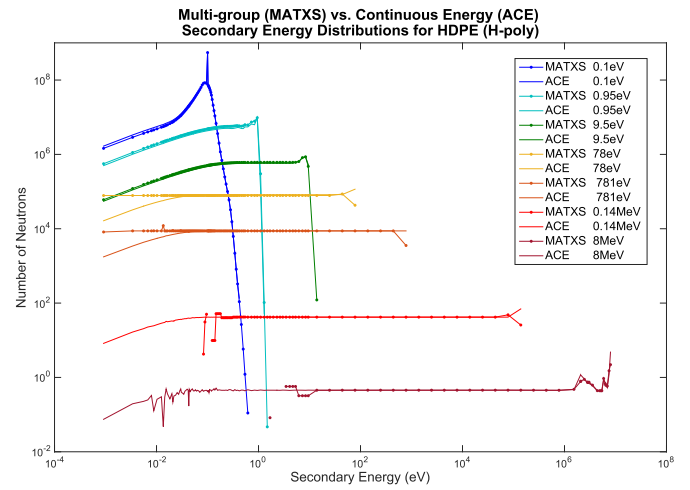**Fig. 5.** Secondary energy distribution for free-gas hydrogen: continuous energy vs. analytic model.
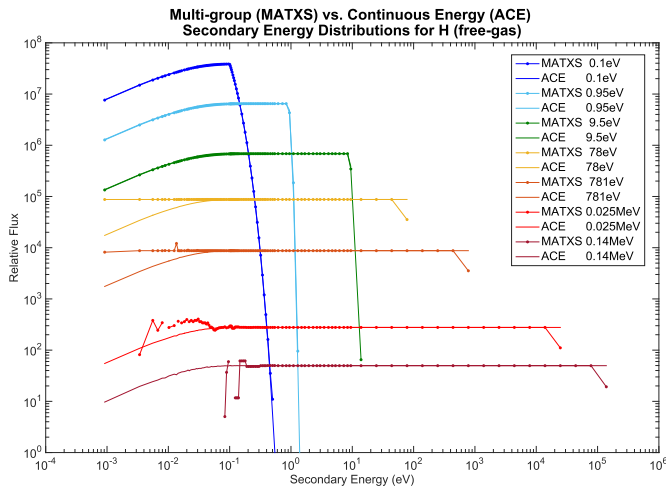

Fig. 6. Secondary energy distribution for free-gas hydrogen: continuous energy vs. multi-group.

free-gas thermal treatment, MCNP does not have its own $S(\alpha,\beta)$ model. Further investigation revealed that MCNP actually uses $S(\alpha,\beta)$ scattering data from the cross section file whenever it is available. In the absence of $S(\alpha,\beta)$ data, it will apply its own free-gas treatment as a substitute for the true $S(\alpha,\beta)$ treatment (Zhang et al., 2017). It won't be as accurate as doing the true $S(\alpha,\beta)$ treatment, but is still better than using static scattering cross section. Finally, the secondary energy spikes near the incident energies are due to neutron scattering off carbon present in the HDPE.

2.3. Testing NJOY with raised thermal cut-off

As we saw in Section 3.1, both our analytic model and MCNP suggest that thermal treatment is non-negligible regardless of the neutron incident energy. NJOY's internal limit on the thermal treatment cut-off will inevitably lead to errors in the neutron slowing-down calculation, mostly for multi-group calculation in deterministic codes as they generally do not have their own thermal treatment models to compensate for lack of thermal scattering data in the cross section files. To better understand the impact of this deficiency, we requested and obtained a temporary patch from LANL to raise the thermal cut-off limit and compared the neutron spectrum of a slowing-down problem before and after the patch.

Fig. 7. Secondary energy distribution for h-poly hydrogen: continuous energy vs. multi-group.

First, to verify the efficacy of the patch, we regenerated the secondary energy distributions for both free-gas and $S(\alpha,\beta)$ treatments. The results are given in Fig. 8 and Fig. 9. They show that the patch successfully raised the internal thermal cut-off limit and NJOY is now able to apply thermal treatment to neutrons with incident energy up to *emax* = 100eV. One problem with the raised cut-off is that, MCNP, as we tested, was not compatible with NJOY generated ACE cross section with *emax* = 100eV. As a compromise, we ran the MCNP simulation with ACE cross sections generated with *emax* = 20eV. Therefore, in Fig. 9, the continuous energy results are actually for *emax* = 20eV. It also explains the difference observed for incident energy of 78eV, where multi-group cross section received full $S(\alpha,\beta)$ treatment while MCNP used internal free-gas treatment in place of $S(\alpha,\beta)$.

For the actual neutron slowing-down problem, we considered an infinite medium of borated HDPE (B-HDPE) with a distributed AmBe neutron source. To compute the slowing-down spectrum, we used PDT (our in-house Parallel Deterministic Transport code) and MCNP. For PDT, the A 138-group energy group structure was designed to resolve the resonance at the high energy end and Bragg edges at the low energy end for carbon cross section. For MCNP, we ran sufficient number of particle histories so that the statistical noise is negligible for comparison purpose. The resulting neutron spectrum is given in Fig. 10. It can be seen that in the slowing-down and fast energy range, PDT results agree
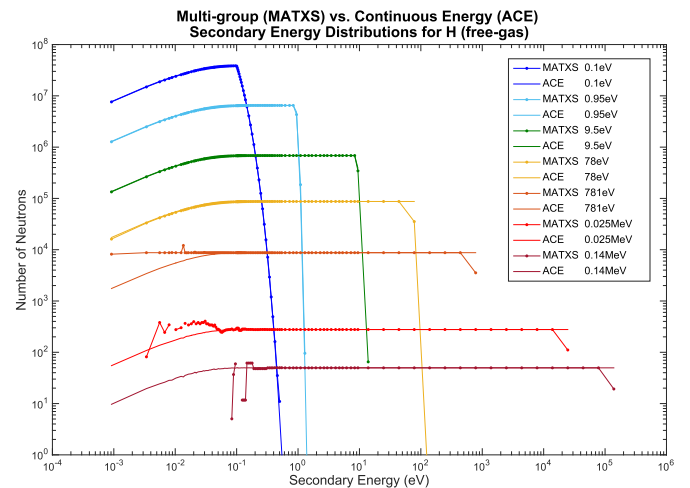

Fig. 8. Secondary energy distribution for free-gas hydrogen: continuous energy vs. multi-group (with LANL patch, reprinted from (Zhang et al., 2017)).
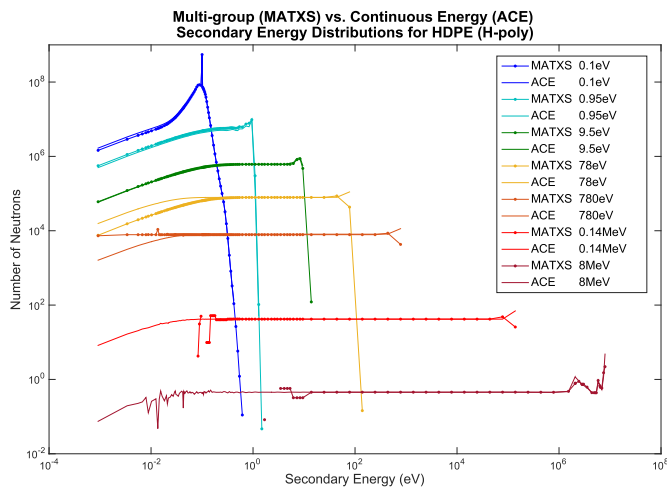
Fig. 9. Secondary energy distribution for h-poly hydrogen: continuous energy vs. multi-group (with LANL patch, reprinted from (Zhang et al., 2017)).

very well with MCNP result. However, towards the low energy end, PDT starts to deviate from MCNP result. The discrepancy is attributed to the insufficient thermal treatment. As we increase *emax*, the PDT result converges to MCNP result monotonically. Particularly, the error reduced by a factor of 6.3 from *emax* = 10eV to *emax* = 100eV. It shows that in this particular type of problems, thermal treatment to higher incident energy can make a significant difference in the thermal neutron population.

3. P_1 Secondary energy distribution for hydrogen scattering

The energy transfer of the P_1 moment is important when the anisotropy in the nuclear system is not negligible. For P_1 secondary energy distribution, we compare analytic model prediction with NJOY multi-group results, as it is not straightforward to obtain P_1 moments from continuous energy cross section data.

3.1. P_1 Moment without thermal treatment

We first looked at the simple case with no thermal treatment, which albeit being simple was rarely investigated explicitly in current literature. To obtain static results, we skipped THERMR module in NJOY and we used Eq. (26) for the analytic model. The results for a variety of incident neutron energies (E) are plotted in Figs. 11–14. It can be seen
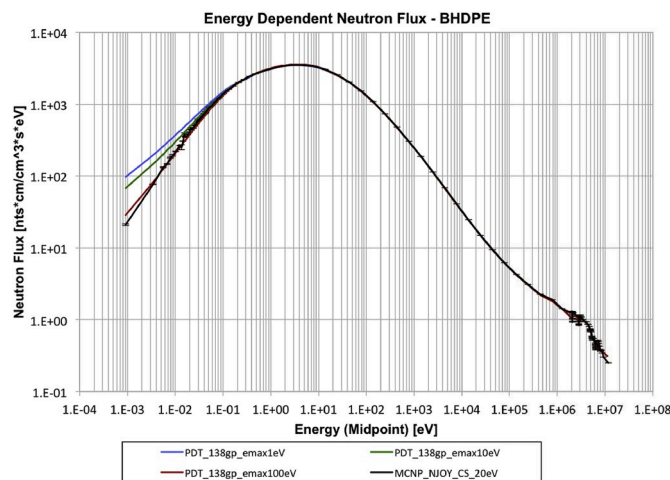

Fig. 10. Neutron spectrum in infinite B-HDPE with AmBe distributed source (reprinted from (Zhang et al., 2017)).

from the figures that NJOY multi-group results agree very well with the analytic model for incident energy below 10eV. Fig. 14 shows that for *E* = 247eV, NJOY's result is lower than analytic result in the mid-to-low energy range. At the very low energy end, a difference of around 47% was observed. This, together with the non-physical oscillation observed in the low energy range, can also be attributed to NJOY's numerical integration artifacts (Zheng and McClarren, 2015).

3.2. P_1 Moment with free-gas thermal treatment

For the free-gas thermal treatment we compared the analytic model and NJOY generated multi-group cross sections for incident energies of 0.5eV, 9.45eV, 44eV, and 247eV. The results are shown in Fig. 15 through Fig. 18, respectively.

Fig. 15 shows that for incident energy of 0.5eV, NJOY's result generally follows analytic model's prediction, except that in the mid-low energy range (around 0.01eV), NJOY gives slightly lower value. Figs. 16 and 17 show that as incident energy increases (from several eV to tens of eV range), NJOY matches the analytic model almost perfectly. Fig. 18 shows that when incident energy exceeds *emax*, NJOY reverts back to static mode, and the difference is huge at the low energy end as compared to the analytic free-gas model. Once again, some spurious oscillations were observed in the low energy region of the NJOY static cross section. It indicates that thermal treatment can make significant difference in the anisotropy of the angular flux when down scattering from incident energy higher than 100eV is non-negligible.

4. Conclusion

In this paper, we extended the two-body kinematics model to obtain analytic expressions for secondary energy distributions for the zero-th (P_0) and the first (P_0) Legendre moments of neutron scattering cross section, as well as its generalization to an arbitrarily higher order. For the P_0 moment, we focused on the free-gas thermal scattering, while for the P_1 moment we looked at both static and free-gas thermal scattering. We compared our analytic model's prediction with NJOY generated secondary energy distribution for the case of hydrogen elastic scattering. Very good agreement was found between the two, with three exceptions: 1) NJOY overestimates static P_1 secondary energy distribution at low energy tail for high incident energy (*E* = 247eV); 2) NJOY slightly underestimates free-gas P_1 secondary energy distribution at low energy tail for low incident energy (*E* = 0.5eV); 3) Some numerical artifacts were observed for high incident energies for both P_0 and P_1 moments. We also discovered a NJOY internal limit of 10eV, beyond which NJOY is unable to perform thermal treatment although our analytic model suggests that thermal treatment is non-negligible. With a patch provided by LANL,
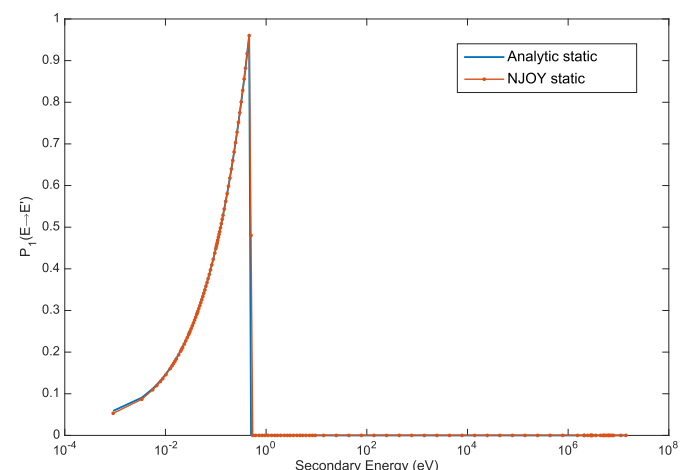

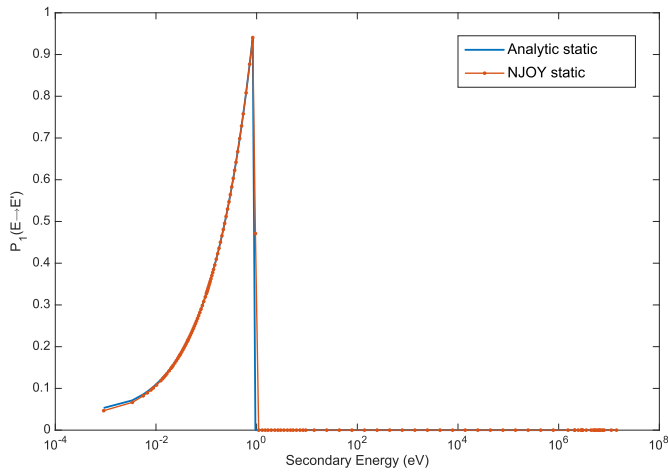**Fig. 11.** Secondary energy distribution for P_1 moment, $E = 0.5$eV.

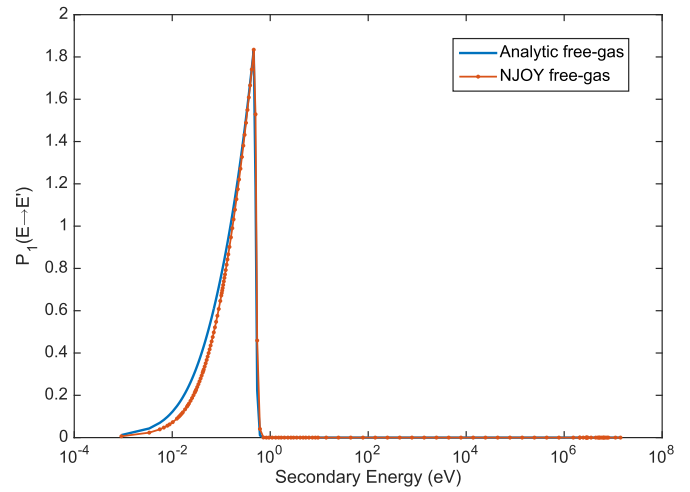**Fig. 12.** Secondary energy distribution for P_1 moment, $E = 0.945$eV.

Fig. 13. Secondary energy distribution for P_1 moment, $E = 5.31$eV.

Fig. 14. Secondary energy distribution for P_1 moment, $E = 247$eV.

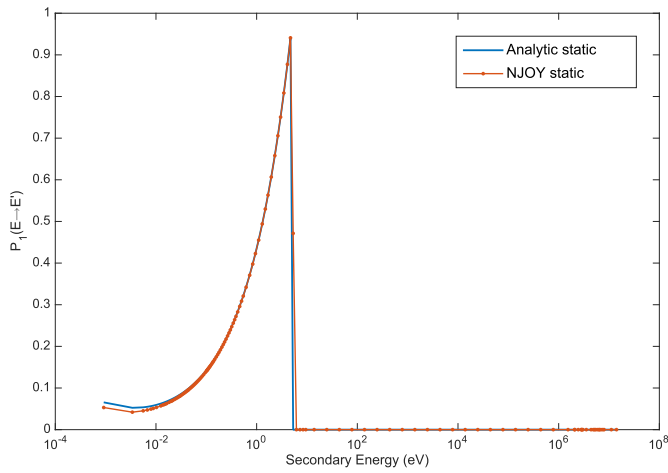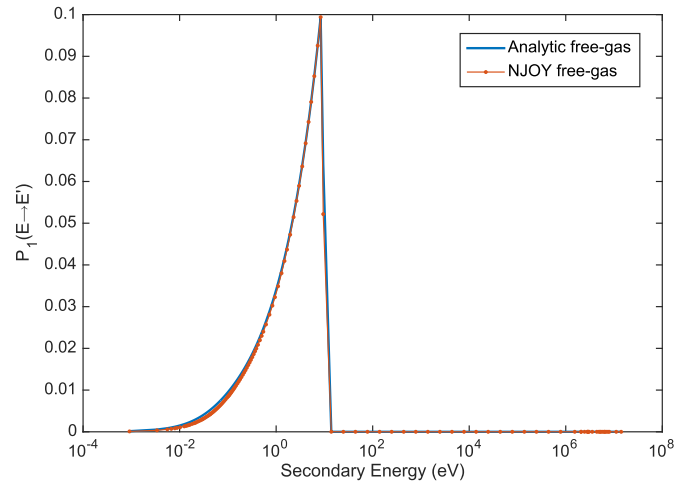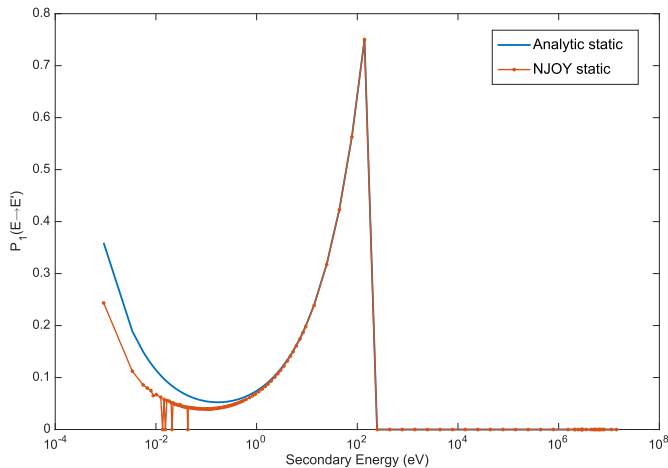**Fig. 15.** Secondary energy distribution for P_1 moment (free-gas), $E = 0.5$eV.

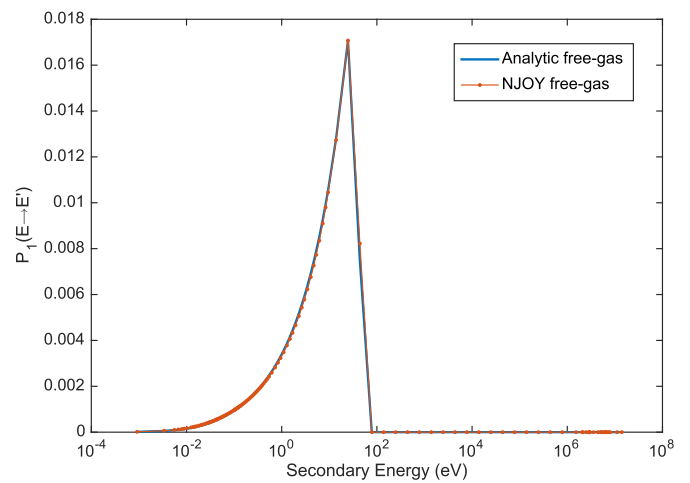**Fig. 16.** Secondary energy distribution for P_1 moment (free-gas), $E = 9.45$eV.

Fig. 17. Secondary energy distribution for P_1 moment (free-gas), $E = 44$eV.

NJOY was able to perform thermal treatment above that limit with satisfying accuracy as judged by the analytic model. When investigating the P_0 moment secondary energy distribution, we employed MCNP as an independent verification, which also suggests that an increase in thermal cut-off is advisable. With the help of MCNP, we further extended our investigation to $S(\alpha, \beta)$ thermal treatment. A slowing-down test problem

in an infinite medium B-HDPE material shows that with increased thermal cut-off, the error in the neutron spectrum at the low energy end reduces by a factor of 6.3 as compared to standard NJOY. Lastly, although the discussion presented in this paper focuses on hydrogen
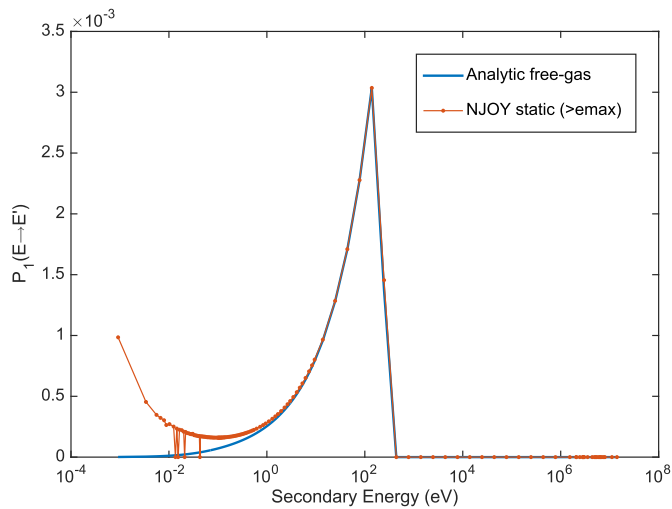
Fig. 18. Secondary energy distribution for P_1 moment (free-gas), $E = 247 \mathrm{eV}$.

scattering (with $A = \frac{1.007276u}{1.008664u} = 0.9986$), the analyses can be generalized to target nuclide with arbitrary atomic mass by substituting in the proper mass ratio A. As a side note, the author would like to point out that although it is adequate to use $A = 1$ in the P_0 moment analytic model, it is crucial that precise A value is used when using the P_1 analytic model, otherwise serious error may result.

Declaration of competing interest

The authors declare that they have no known competing financial interests or personal relationships that could have appeared to influence the work reported in this paper.

CRediT authorship contribution statement

Yunhuang Zhang: Formal analysis, Investigation, Writing - original draft, Writing - review & editing, Visualization. **Marvin L. Adams:** Conceptualization, Supervision.

Acknowledgement

Appendix A. Supplementary data

Supplementary data to this article can be found online at https://doi.org/10.1016/j.pnucene.2020.103379.

References

Bell, G.I., Glasstone, S., 1985. Nuclear Reactor Theory, third ed. Krieger Pub Co, Princeton, NJ.

Conlin, Jeremy Lloyd, Kahler, A.C., McCartney, Austin P., Rehn, Daniel A., 2017. Njoy21: next generation nuclear data processing capabilities. EPJ Web Conf. 146, 09040.

Lamarsh, J.R., Baratta, A.J., 2001. Introduction to Nuclear Engineering, third ed. Pearson.

MacFarlane, R.E., 2013. The Njoy Nuclear Data Processing System, Version 2012. Los Alamos National Laboratory. Tech. Rep. LA-UR-12-27079.

Y. Zhang, A. J. Holzaepfel, and M. L. Adams, "Njoy maximum energy limit for thermal neutron cross section treatment," in M&C 2017 - International Conference on Mathematics & Computational Methods Applied to Nuclear Science & Engineering, (Jeju, Korea), American Nuclear Society, April 16-20 2017.

Zheng, W., McClarren, R.G., 2015. Semi-analytic benchmark for multi-group free-gas legendre moments and the application of gauss quadrature in generating thermal scattering legendre moments. Ann. Nucl. Energy 85, 1131–1140.